Land Surface Controls on Hydroclimatic Means and Variability

RANDAL D. KOSTER

Global Modeling and Assimilation Office, NASA Goddard Space Flight Center, Greenbelt, Maryland

SARITH P. P. MAHANAMA

Global Modeling and Assimilation Office, NASA Goddard Space Flight Center, Greenbelt, and Science Systems and Applications, Inc., Lanham, Maryland

(Manuscript received 30 March 2012, in final form 22 June 2012)

ABSTRACT

Hydroclimatic means and variability are determined in large part by the control of soil moisture on surface moisture fluxes, particularly evapotranspiration and runoff. This control is examined here using a simple water balance model and multidecadal observations covering the conterminous United States. Under the assumption that the relevant soil moisture–evapotranspiration and soil moisture–runoff relationships are, to first order, universal, the simple model illustrates the degree to which they interact to determine spatial distributions of hydroclimatic means and variability. In the process, the simple model provides estimates for the underlying relationships that operate in nature. The hydroclimatic sensitivities established with the simple water balance model can be used to evaluate more complex land surface models and to guide their further development, as demonstrated herein with an example.

1. Introduction

Budyko (1974) provided a simple framework for describing the control of climatic forcing on hydroclimatic regime, showing how the relative levels of water and energy availability in a region help determine the region's mean annual evaporation and runoff rates. Underlying this framework is the recognition that evaporation is not always water limited—when the soil is wet enough, evaporation no longer varies with soil moisture; it varies instead with incident energy. Eagleson (1978), in his more comprehensive analysis of hydroclimatology, addressed a number of additional controls on evaporation and runoff, including storm and interstorm properties and soil and vegetation properties. Milly (1994) added to the discussion, elucidating the role of intraseasonal soil water storage.

Numerical climate models generally capture these aspects of hydroclimatology (Koster et al. 2001; Dirmeyer et al. 2006) largely through their formulations of large-scale land surface physics, that is, through their land surface model (LSM) components. An LSM performs two key sets of calculations at every time step of a weather or climate simulation: (i) surface water balance calculations in which precipitation (P) is partitioned into evaporation (E), runoff (Q), and ground moisture storage and (ii) surface energy balance calculations in which net radiative energy (R_{net}) is partitioned into latent heat flux (λE, where λ is the latent heat of vaporization), sensible heat flux, and ground heat storage. In this paper we are especially interested in the control of a LSM soil moisture variable W (or variables W_n) over the production of evaporation and runoff. This control is sometimes hardwired into the LSM in a very simple way (e.g., the standard ''bucket'' model of Manabe 1969). More often the relevant formulations are much more complex but, even with this complexity, an LSM still tends to generate an evaporative fraction (the fraction of net radiative energy released as latent heat, $\lambda E/R_{\mathrm{net}}$) that either increases with W or, for the energy-limited evaporation regime, is insensitive to it. A common overall behavior is also seen with the runoff ratio (the fraction of incident precipitation that becomes runoff, Q/P); the runoff ratio in LSMs, despite being the product of complex parameterizations, can be characterized as generally increasing with W.

Corresponding author address: Randal Koster, Code 610.1, NASA/GSFC, Greenbelt, MD 20771.
E-mail: randal.d.koster@nasa.gov

DOI: 10.1175/JHM-D-12-050.1

© 2012 American Meteorological Society

The behavior and realism of LSMs has been evaluated extensively over the years (e.g., Wood et al. 1998; Boone et al. 2004; Guo et al. 2006). The particular idea that complex LSM formulations can be examined with simple surrogate relationships was explored in detail by Koster and Milly (1997, hereafter KM97) as part of the Project for the Intercomparison of Land surface Parameterization Schemes (PILPS) (Henderson-Sellers et al. 1993). PILPS was an experiment in which a number of LSMs were driven offline (unconnected from a host GCM) with prescribed meteorological forcing. Using PILPS data, KM97 computed regression lines between soil moisture and both the ratio of evaporation to potential evaporation (similar to $\lambda E/R_{\mathrm{net}}$) and the runoff ratio ($Q/P$). Then they applied those simple fitted relationships within a simple monthly water balance model (MWBM) driven with the same forcing. The MWBM was found to reproduce well the average behavior of the more complex LSMs, demonstrating that it indeed captured the fundamental controls imposed by each LSM on the surface water budget (and thus, through the evaporation connection, on the surface energy budget). In other words, the fitted $\lambda E/R_{\mathrm{net}}$ and Q/P relationships were found to characterize, to first order, the more complex formulations in the LSMs, allowing KM97 to explain the different mean behaviors of the PILPS LSMs in terms of these simpler relationships.

The KM97 analysis of LSM behavior focused on simulated hydroclimatic means. The usefulness of climate models naturally also depends on their ability to simulate hydroclimatic *variability* (droughts and pluvial periods, interannual variations in streamflow, etc.). Many studies have examined hydroclimatic variability in the context of broad climatic controls (e.g., Koster and Suarez 1999; Roderick and Farquhar 2011) or nonstationary background statistics (e.g., Nemec and Schaake 1982; Milly et al. 2008). In this paper, we examine hydroclimatic means and variability jointly in the context of land surface processes, using a strategy akin to that of KM97. We devise a simple water balance model that captures the control of soil moisture over evaporation and runoff and then use the model to show how the nature of this control manifests itself in hydroclimatic statistics. Unlike KM97, we evaluate the results of the present study against observations.

Following a description of our simple water balance model in section 2 and the presentation of observations-based estimates of hydroclimatic means and variability in section 3, section 4 illustrates the strong sensitivity of hydroclimatic statistics to the structure of the relationships between $\lambda E/R_{\mathrm{net}}$ and W and between Q/P and W. In section 5, we use observations-based fields to provide estimates for the $\lambda E/R_{\mathrm{net}}$ and Q/P relationships operating in nature. Finally, in section 6, we demonstrate that the simple model results have utility for the improvement of state-of-the-art LSMs used in simulations of climate.

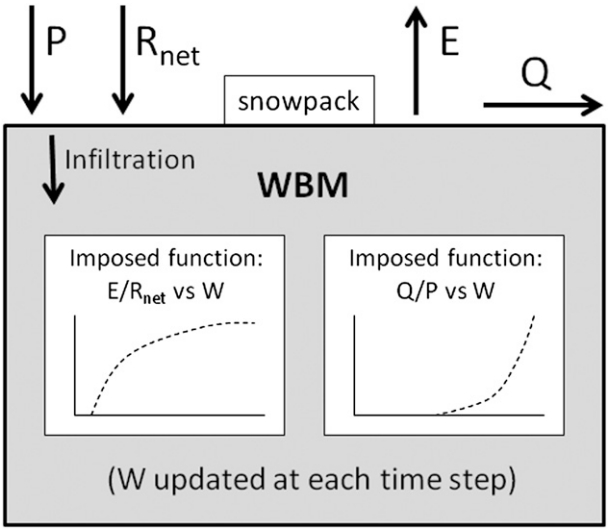

FIG. 1. Schematic of the water balance model (WBM) used in this study. The forcing variables, imposed daily, are precipitation (P) and net radiation (R_{net}); the WBM uses the imposed evaporation and runoff relationships to compute the daily evaporation (E) and runoff (Q) as a function of its prognostic water content (W). See text for details.

2. Description of the water balance model

Figure 1 shows a schematic of the simple water balance model (WBM) used in this study. The model uses a time step of one day. On each day, observations-based values of precipitation and net radiation are imposed on the land surface. A prescribed relationship between Q/P and W (the degree of saturation: the model's main prognostic variable) is used to determine how much of the rainfall leaves the system as runoff; the remainder of the precipitation water infiltrates the soil and updates W. A prescribed relationship between $\lambda E/R_{\mathrm{net}}$ and W is then used to compute the evaporation of water out of the system for the day, and W is updated further. The water-holding capacity of the WBM is arbitrarily set to 337.5 mm and represents, for example, a soil element with a depth of 1 m, a porosity of 0.45, and a wilting point at a degree of saturation of 25%. Results with alternative water-holding capacities (not shown) are quantitatively different but qualitatively the same, particularly in terms of how the WBM's ability to reproduce observations (discussed below) varies with the prescribed $\lambda E/R_{\mathrm{net}}$ and Q/P relationships. The 337.5-mm water-holding capacity used here provides for a relatively

high agreement with the observations and is thus a reasonable choice.

Precipitation water that falls when the surface temperature is subfreezing (based on an observational monthly climatology) is added to a snowpack variable and does not infiltrate the soil or run off the surface. This snowpack melts uniformly in time over the first 20 days of the first month in which the average monthly temperature exceeds 0°C, and the snowmelt water on each day is added to that day's precipitation water. (The use of 20 days here is arbitrary, with other choices producing essentially equivalent results; indeed, the presence of the snow layer itself is found to have little qualitative impact on our results.) Two additional features were considered for inclusion—one to treat interception loss explicitly and the other to separate surface runoff production from baseflow production. While including these options would have the advantage of being more realistic, neither turn out to change our results significantly, presumably because our precipitation inputs are not intermittent (see below) and all of our analyses focus on long-term totals. Given our desire to keep the WBM as simple as possible (i.e., to minimize our degrees of freedom), we do not utilize the interception and the baseflow options in this study.

The WBM is run across the conterminous United States (CONUS) at a spatial resolution of 2.5° × 2.5°. We prescribe the $\lambda E/R_{\mathrm{net}}$ and Q/P relationships using simple second-order polynomials, thus stepping beyond the linearizations employed by KM97. (The actual functions used are piecewise combinations of polynomial and linear functions that ensure acceptable ranges for the computed values and that allow for the distinction between soil moisture-controlled and atmosphere-controlled evaporation regimes. The variety of functions examined will be illustrated explicitly with the WBM results.) The WBM is driven with an array of observations-based precipitation forcing compiled by the University of Washington (Andreadis et al. 2005); here, we use monthly precipitation totals aggregated to 2.5° × 2.5° from this dataset and covering the period 1948–2000. The same precipitation rate is applied on each day of a given month. While the monthly precipitation rates vary interannually, the net radiation inputs do not; we employ a seasonal climatology of net radiation derived from the Surface Radiation Budget (SRB) dataset (Gupta et al. 2006). Driven with this forcing, the WBM simulation produces 53 years of daily evaporation and runoff rates and daily updates to its soil moisture variable; we analyze the final 52 years of these data below.

The WBM's very simple structure is designed to elucidate the primary controls imposed by the land surface on hydroclimatic means and variability. The simplicity naturally requires a number of assumptions that must be kept in mind while interpreting the results. First, the WBM does not perform energy balance calculations and thus could not serve as a land component in a full climate simulation. Second, we are assuming in our simulations that the same $\lambda E/R_{\mathrm{net}}$ and Q/P relationships hold across CONUS and across seasons, thus ignoring, for example, differences in the character of runoff generation in mountainous and flat areas or in the character of evaporation before and after leaf out. Other relevant assumptions include the lack of high frequency precipitation intermittency and the avoidance of explicit treatments of baseflow and interception. While these assumptions, particularly the second one, may seem harsh, they appear to have only a second-order impact on our results, as shown in sections 5 and 6.

3. Observations-based distributions of hydroclimatic means and variability

Our analysis of hydroclimatic means and variability will focus on the four fields illustrated in Fig. 2. The first field, shown in Fig. 2a, is the mean runoff ratio across 23 large-scale basins mostly in the continental United States. The streamflow data used to generate the plot, along with basin and stream gauge characteristics, are described in detail by Mahanama et al. (2012). Basically, the data consist of multiple decades of naturalized streamgauge observations averaged to annual totals. In an additional processing step, streamflow measurements between any two consecutive gauges on the same river are differenced before the means are computed so that the plotted means for the upstream and downstream gauges are independent. (The runoff areas contributing to each mean calculation are accordingly independent and are plotted as separate areas in the figure.) Clearly seen are larger ratios in the east and in some mountainous basins in the far west. Note that the concept of higher streamflows in the east, where precipitation is larger, is trivial; here the map shows something more subtle: the ratio of streamflow to precipitation is also larger, in accordance with the Budyko (1974) framework.

The runoff ratios in Fig. 2a constitute the observational data used to evaluate our simulations of large-scale hydroclimatic means. To evaluate our simulations of hydroclimatic variability, we use the observations-based fields presented in Figs. 2b–d. By focusing on the spatial patterns of variability rather than on its absolute magnitude, we make use of three fully independent sets of observations.

The first field, in Fig. 2b, is the spatial distribution of total annual streamflow variance over the 23 indicated large-scale basins, as computed from the same data used

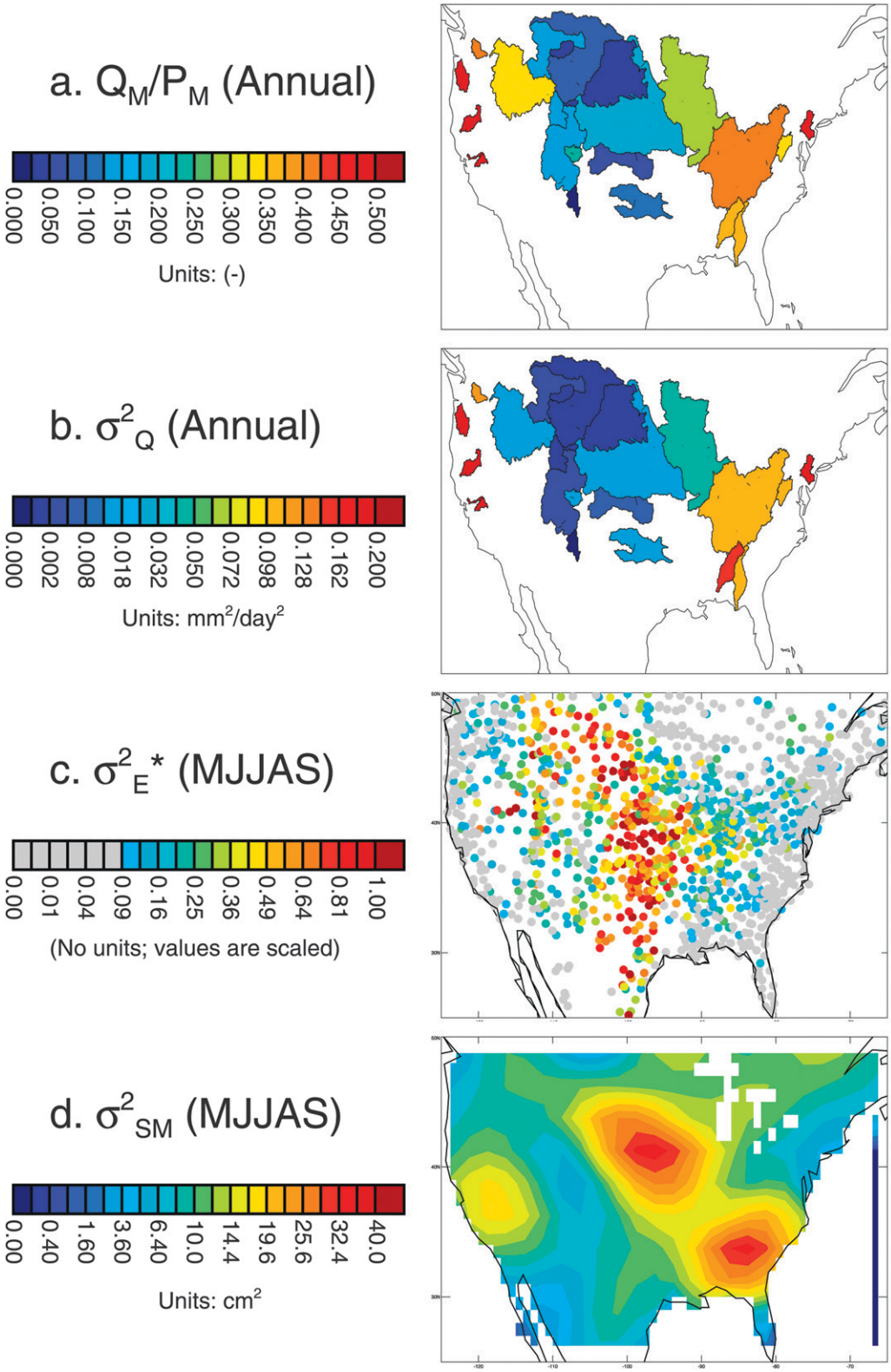

FIG. 2. Measures of hydrological means and variability, as derived from observations: (a) the annual streamflow divided by the annual precipitation in the indicated basins, (b) the interannual variance of runoff ($mm^2\ day^{-2}$) as derived from streamflow observations, (c) the interannual moisture-related variance of MJJAS evaporation (no units) as derived from temperature measurements (see appendix), (d) and the interannual variance of MJJAS land water content (cm^2) as derived from GRACE data.

to create Fig. 2a. For Fig. 2b, annual streamflows were computed over the period from October to September, reflecting a common definition of ''water year.'' Higher variances appear, as expected, toward the east, where rainfall variances (not shown) are larger. Note that, in contrast to Fig. 2a, the streamflow data here are not normalized by precipitation.

Figure 2c shows a proxy (temperature based) estimate of the spatial distribution of σ_E^2* over North America, where σ_E^2* is defined as the interannual variance of May–September (MJJAS) evaporation totals associated with variations in water availability:

$$\sigma_E^2* = \sigma_E^2 r^2(E, P_{\mathrm{ann}}), \tag{1}$$

where σ_E^2 is the total variance of MJJAS E and $r^2(E, P_{\mathrm{ann}})$ is the square of the correlation coefficient between MJJAS E and P_{ann}, the total precipitation from October of the preceding year through September of the current year. Here, we employ the standard interpretation of $r^2(E, P_{\mathrm{ann}})$ as the fraction of the variance of E ''explained'' by variations in P_{ann} and thus by variations in water availability; under this interpretation, when σ_E^2 is multiplied by $r^2(E, P_{\mathrm{ann}})$, we obtain an estimate for the ''moisture related'' portion of σ_E^2. That is, the equation allows us to isolate this part of evaporation variability from that associated with other sources, such as variations in radiation or humidity. See appendix for a discussion of how historical temperature and precipitation observations are used here as proxies for historical evaporation and soil moisture observations, respectively, in the generation of the figure. We note that this evaporation variance pattern is consistent with the much coarser evaporation variance pattern (not shown) inferred from estimating annual evaporation as the difference between annual precipitation and streamflow within the gauged basins and is also very similar to the pattern derived (not shown) from indirect evaporation estimates produced by Jung et al. (2010) using FluxNet observations, remote sensing data, and gridded observational forcing.

Finally, Fig. 2d shows the spatial distribution of the interannual variance of average MJJAS land water storage, as derived from nine years of Gravity Recovery and Climate Experiment (GRACE) data by Swenson and Wahr (2006). GRACE consists of a pair of satellites that measure variations in the earth's gravity field—variations that in turn can be processed into temporal anomalies in total water storage [soil moisture, snow, groundwater, and surface water; Tapley et al. (2004)]. Although the sample space from which these variances are produced is quite small, inclusion of the GRACE data was deemed important to this study given our focus on the shapes of the $\lambda E/R_{\mathrm{net}}$ and Q/P relationships. Evaporation or runoff variability is controlled not only by the slopes of these relationships but also by the soil moisture range over which these slopes act; for a given slope, a larger range (i.e., a larger soil moisture variance) implies a larger evaporation or runoff variability. The GRACE data show two main bullseyes of water content variance—one in the central United States and one in the southeastern United States. Such a pattern is similar to the observed spatial pattern of warm-season precipitation variance (shown for July, for example, by Koster et al. 2003).

4. Results: Sensitivity of hydroclimatic means and variability to imposed relationships

The WBM produces data that can be processed into statistics corresponding to those shown in Fig. 2 for the observations. Daily runoffs from the WBM are aggregated from October through September to generate 52 annual totals from which we compute the mean runoff ratio and runoff variances for each hydrological basin. (As with the observations, mean runoff ratio is computed as the ratio of the long-term mean streamflow to the long-term mean precipitation and not as the mean of the individual yearly ratios.) For comparison with Fig. 2c, the daily evaporation rates produced by the WBM are aggregated into May–September averages, and evaporation variances and correlations between MJJAS evaporation and annual precipitation are computed from the resulting sets of 52 yearly values. The 52 simulated MJJAS W values are combined with the imposed water-holding capacity to generate the WBM fields of σ_W^2.

Figure 3 presents results for a particular set of four WBM experiments. The leftmost column shows the four pairs of $\lambda E/R_{\mathrm{net}}$ and Q/P relationships used (the red and blue curves, respectively, in a given panel); the four experiments (one per row) are seen to differ only in their imposed evaporation function. In the first experiment (the first row), the maximum ratio of $\lambda E/R_{\mathrm{net}}$ is 0.4. The subsequent experiments have progressively higher maximum ratios (indicating an increasing ease of generating evaporation), up to a value of 1 for the fourth experiment (the final row). The second column in the figure shows the resulting spatial distributions of basin-level Q_M/P_M (i.e., the mean annual runoff divided by the mean annual precipitation), the third shows σ_Q^2, the fourth shows the gridcell-level distribution of σ_E^2*, and the fifth shows the corresponding spatial distribution of σ_W^2.

Marked on the σ_E^2* plots (fourth column) are the locations of two representative grid cells—one in the west (''Y'') and one in the east (''Z''). Plotted in orange above the $\lambda E/R_{\mathrm{net}}$ and Q/P relationships in the first column is an indication, for each of these two points, of

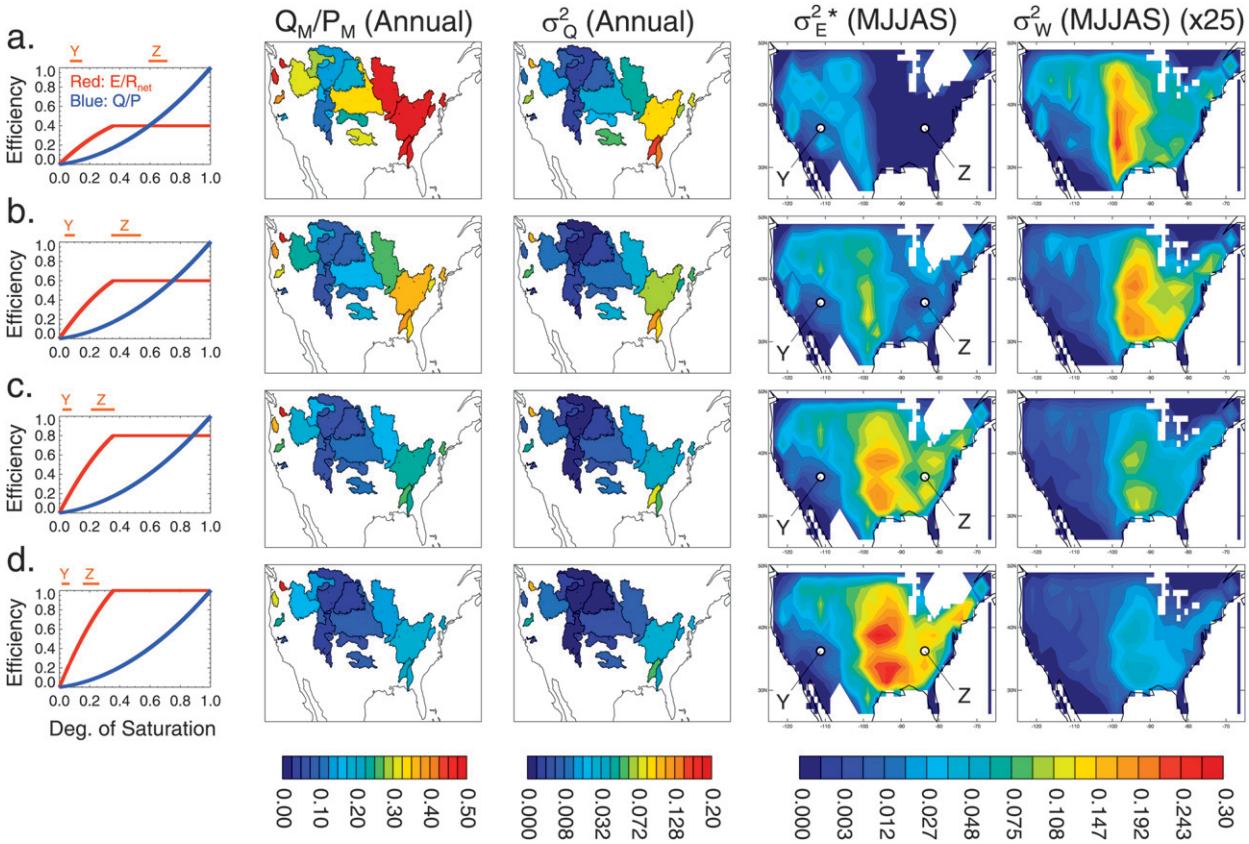

FIG. 3. Impact of the "height" of the $\lambda E/R_{\mathrm{net}}$ relationship on hydrological means and variability: (a) plots showing (from left to right) the imposed pairing of $\lambda E/R_{\mathrm{net}}$ and Q/P relationships in a specific WBM experiment and the resulting spatial distributions of average runoff ratio (Q_M/P_M) in individual basins (dimensionless), σ_Q^2 in individual basins (mm^2 day^{-2}), σ_E^2* (mm^2 day^{-2}), and σ_W^2 (cm^2). Notice that σ_W^2 has been multiplied by 25 prior to plotting to allow visualization of the patterns with the same color bar. A rough indication of the soil moisture ranges experienced during May–September at the points labeled Y and Z in the fourth column is shown just above the plot in the first column; each range drawn corresponds to the daily mean plus or minus one standard deviation. (b)–(d) As in (a) but for a (b) second, (c) third, and (d) fourth experiment.

the range of daily soil moistures experienced by the WBM during May through September. To avoid overlap, the full range is not plotted; shown is the range represented by the mean daily soil moisture plus or minus one standard deviation.

Since the evaporation function is modified in this set of experiments, we focus on the evaporation response (the fourth column) first. Clearly, as the height (i.e., the maximum value) of the $\lambda E/R_{\mathrm{net}}$ relationship increases, the moisture-dependent evaporation variance (σ_E^2*) increases, especially in the eastern half of the United States. To a large extent, this reflects concomitant increases in the mean evaporation; such increases in the mean are intuitive and, while not shown here explicitly, are reflected in the second column, which shows a decrease in Q_M/P_M with the height of the $\lambda E/R_{\mathrm{net}}$ relationship. Changes in the mean evaporation, however, do not explain all of the changes seen in σ_E^2*; the shape of the evaporation function has its own impact, as confirmed by an analysis of coefficients of variation (not shown). In Fig. 3a, soil moisture in the eastern half of the continent is high, in the regime for which it does not affect evaporation (as indicated in the first panel for the representative gridcell Z). Values of σ_E^2* there are thus low for that reason alone. As the height of the $\lambda E/R_{\mathrm{net}}$ relationship increases (Figs. 3b–d), evaporation itself increases. This translates the active soil moisture range toward drier values, further into the regime for which evaporation *does* vary with soil moisture content (see the shift in the indicated range for gridcell Z). Evaporation variability is thereby increased.

The runoff variance (third column in Fig. 3) decreases as the evaporation variability increases. This complementary behavior is expected given that long-term-average precipitation is balanced by the sum of long-term-average runoff and evaporation. Keep in mind, however, the

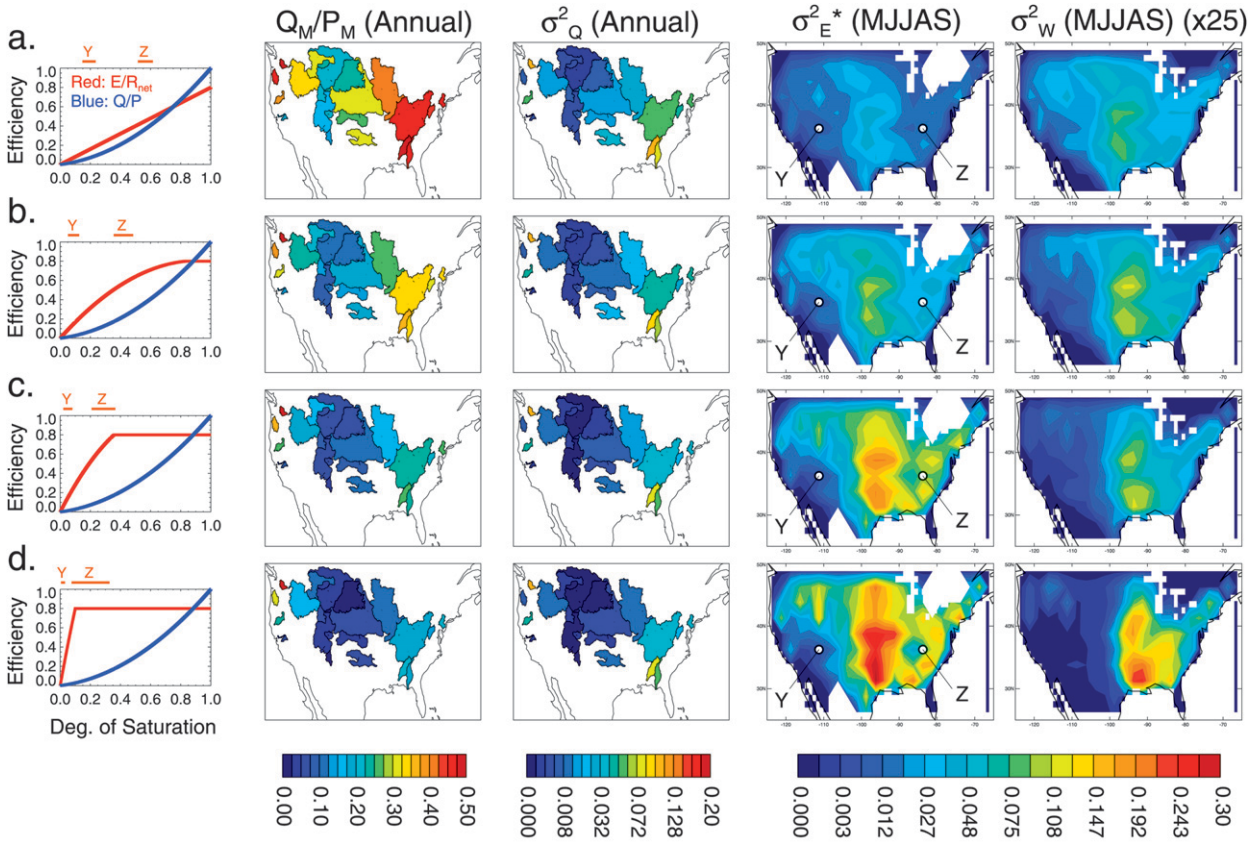

FIG. 4. Impact of the shape of the $\lambda E/R_{\mathrm{net}}$ relationship on hydrological means and variability: panels as in Fig. 3.

different averaging periods for evaporation and runoff in the figure.

The distribution of soil moisture variance (final column) shows two features of interest. First, an increase in the height of the $\lambda E/R_{\mathrm{net}}$ relationship leads to a reduction in the soil moisture variance. Second, and more important given our focus on the spatial distribution of σ_W^2 as opposed to its absolute magnitude, the increase in the height of the $\lambda E/R_{\mathrm{net}}$ relationship leads to a less sharply defined maximum of σ_W^2 in the center of the continent.

Figure 4 shows how the general shape, as opposed to the height, of the $\lambda E/R_{\mathrm{net}}$ relationship affects the hydroclimatic statistics. Here we quantify the sensitivities to the location of the transition point between soil-moisture-controlled and energy-controlled evaporation, with this transition point moving to drier soil moistures in the progression of experiments. As in Fig. 3, the imposed Q/P function is identical in all four experiments. Figure 4 shows that evaporation variance, particularly in the center of the continent, tends to increase as the transition point is moved toward drier soil moistures—partially a reflection of the increase in evaporation (as reflected by the decrease in Q_M/P_M) but also a reflection of the higher slopes imposed in the soil-moisture-controlled evaporation regime and the ability of the higher evaporation rates to push soil moistures into this regime. As expected, the runoff variances decrease as the evaporation variances increase. Soil moisture variances increase in the east and decrease in the west in the progression of experiments.

Figure 5 shows the impact of changing the runoff function while keeping the evaporation function constant. Only in the first two experiments (Figs. 5a and 5b) is runoff produced for all values of soil moisture. Runoff production is made more and more difficult in the progression of experiments (Figs. 5a–d); in the final experiment (Fig. 5d), for example, runoff is produced only when W exceeds 0.75.

In this set of experiments, western evaporation variances increase and runoff variances decrease slightly as runoff production is made more difficult. These results make intuitive sense: the runoff ratio itself decreases (second column), and changes in variance do tend to follow, to some extent, changes in the mean. Again, however, there is much more to the story; variability is

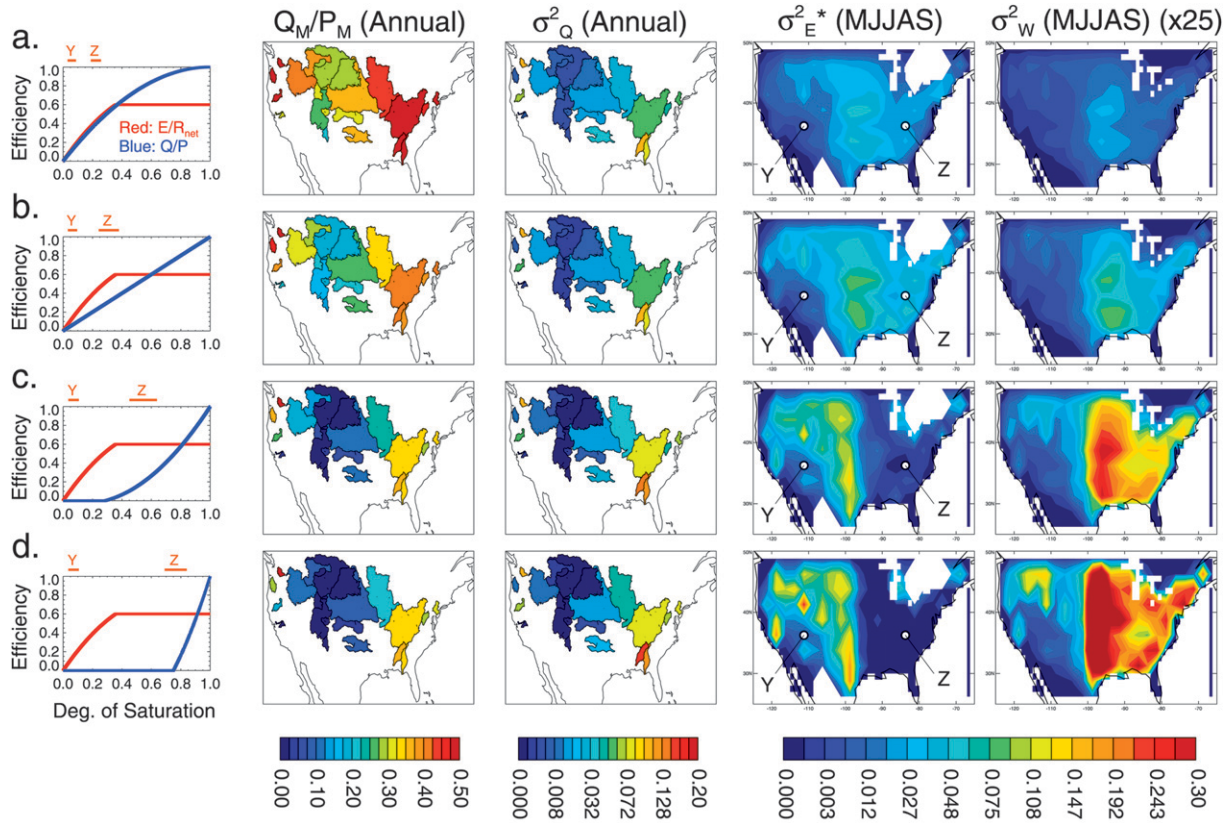

FIG. 5. As in Fig. 4 but showing the impact of the shape of the Q/P relationship.

also controlled by the *shapes* (e.g., the slopes) of the imposed functions. The W values in the west are generally low, and the progression of experiments in Fig. 5 (first column) shows a decreasing Q/P-versus-W slope in the dry regime. Runoff variances for this regime, which partially reflect these slopes, thus decrease in the progression of experiments, and evaporation variances increase accordingly. Such arguments regarding changes in slope are, in fact, essential in the east where runoff variance increases in the progression of experiments even as the mean runoff decreases. In contrast to the dry regime, the wetter regime features an *increasing* Q/P-versus-W slope as runoff production is made more difficult, encouraging higher values of σ_Q^2. For the final experiment (Fig. 5d), the high slope only operates in the $0.75 < W < 1$ range; however, for this experiment, the lower runoff rates help nudge the soil moistures into this wet range (see the shift in the range for the representative grid cell Z). Notice that soil moisture variances increase almost everywhere as runoff production is made more difficult.

The three sets of experiments in Figs. 3–5 are not meant to be comprehensive; they are provided as examples to illustrate how the shapes of the imposed evaporation and runoff functions translate into various facets of simulated hydroclimatic fields. They are also presented to show how evaporation statistics are not controlled solely by evaporation formulations, and how runoff statistics are not controlled solely by runoff formulations. One result is particularly intriguing: the time variability of runoff (σ_Q^2) appears to be affected more by changes in the evaporation function (Fig. 3) than by changes in the runoff function (Fig. 5). Of course, the magnitudes of the imposed changes in the evaporation and runoff functions cannot be objectively compared; still, the range of runoff functions examined in Fig. 5 is substantial.

5. Implications for evaporation and runoff behavior in nature

Figure 2 provides a first-order indication of the spatial patterns of Q_M/P_M, σ_Q^2, $\sigma_E^2{*}$, and σ_W^2 present in nature. Figures 3–5 provide contrasting spatial patterns of Q_M/P_M, σ_Q^2, $\sigma_E^2{*}$, and σ_W^2 for different choices of evaporation and runoff functions; some of these patterns look more realistic, relative to Fig. 2, than others. By testing a

more comprehensive set of evaporation and runoff function combinations with the WBM, we could use Fig. 2 to establish the particular pairing that best reproduces the mean and variability distributions seen in the observations. The determination of such an optimal pairing would identify the evaporation and runoff functions that best represent (to within the limits of our assumptions) the functions operating in nature.

We attempt such a determination here. We perform a large number of WBM simulations with a more comprehensive variety of $\lambda E/R_{\mathrm{net}}$ and Q/P relationships, and for each simulation we evaluate how well the patterns of hydroclimatic statistics agree with observations.

Given that direct evaporation measurements on the continental scale are unavailable, and because GRACE data reflect changes over the entire snow–soil–aquifer column rather than over the depth represented by the WBM (and are, in any case, provided as anomalies), we use the streamflow measurements alone to evaluate the WBM reproduction of hydroclimatic means. That is, we quantify the ability of a given pairing of $\lambda E/R_{\mathrm{net}}$ and Q/P relationships to reproduce the mean runoff ratios in the 23 basins shown in Fig. 2a. More specifically, we compute $\langle \mathrm{RMSE}(Q_M/P_M)\rangle$, the area-weighted root-mean-square error of the WBM estimation of runoff ratio, Q_M/P_M:

$$\langle \mathrm{RMSE}(Q_M/P_M)\rangle = \{\Sigma_{\mathrm{basin}} A_{\mathrm{basin}}[(Q_{\mathrm{sim},M}/P_M) - (Q_{\mathrm{obs},M}/P_M)]^2/\Sigma_{\mathrm{basin}} A_{\mathrm{basin}}\}^{1/2}. \quad (2)$$

Here $Q_{\mathrm{sim},M}$ and $Q_{\mathrm{obs},M}$ are simulated and observed annual mean streamflows for a given basin, P_M is the annual mean precipitation in the basin, and A_{basin} is the basin area. Because both modeled and observed runoff ratios lie between 0 and 1, a $\langle \mathrm{RMSE}(Q_M/P_M)\rangle$ close to 1 (i.e., a large average RMSE) implies a poor reproduction of mean runoff ratio. A $\langle \mathrm{RMSE}(Q_M/P_M)\rangle$ of 0, of course, implies a perfect reproduction.

For three of the very small basins shown on the far western coast (viz., those associated with the stream gauges for the San Joaquin River at Mokelunme Hill, for the Tuolumne River at La Grange Dam, and for the Willamette River near Oregon City; see Mahanama et al. 2012 for details), no combination of evaporation and runoff functions allowed a local runoff ratio RMSE of less than 0.53. We interpret this as a severe inconsistency between the independently measured streamflow and precipitation data in the basin, and we remove these three basins from consideration.

Figure 6 shows how $\langle \mathrm{RMSE}(Q_M/P_M)\rangle$ varies with the tested combinations of evaporation and runoff function. In fact, the precise quantity plotted here is 1 minus $\langle \mathrm{RMSE}(Q_M/P_M)\rangle$ so that higher values indicate greater skill. (Because $\langle \mathrm{RMSE}(Q_M/P_M)\rangle$ itself is constrained to lie between 0 and 1, 1 minus $\langle \mathrm{RMSE}(Q_M/P_M)\rangle$ also lies between 0 and 1, with a value of 1 implying perfect skill.) The red curves in the top row of a panel show the prescribed $\lambda E/R_{\mathrm{net}}$ relationships used, and the blue curves in the left column show the prescribed Q/P relationships. Skill for a given combination is indicated by the color of the cell in the corresponding column and row. Overall, 252 different pairings of $\lambda E/R_{\mathrm{net}}$ and Q/P relationships are examined here. A number of relationship combinations (e.g., that correspond to the cell labeled B) are seen to provide relatively large values of 1 minus $\langle \mathrm{RMSE}(Q_M/P_M)\rangle$. The cell marked with an X in the top panel identifies the combination that produces, in the WBM, the best reproduction of hydroclimatic means.

To examine the WBM reproduction of the spatial distributions of hydroclimatic variability, we define a composite skill score, S_V, that characterizes the ability of a given combination of $\lambda E/R_{\mathrm{net}}$ and Q/P relationships to reproduce the spatial patterns in Figs. 2b–d:

$$S_V = (r_Q^2 + r_E^2 + r_W^2)/3. \quad (3)$$

The quantity r_Q^2 is the square of the spatial correlation between the WBM-generated distribution of annual basin runoff variance and the distribution in Fig. 2b (removing from consideration the three aforementioned questionable basins), with areal weights applied in the calculation. The term r_E^2 is the square of the spatial correlation between the WBM-generated distribution of $\sigma_E^2{}^*$ (for MJJAS, as in Figs. 3–5) and the observed (proxy) pattern in Fig. 2c. (The station data in Fig. 2c are aggregated to the WBM 2.5° × 2.5° resolution prior to computing this correlation.) Finally, r_W^2 is the square of the spatial correlation between the WBM-generated MJJAS soil moisture variance pattern and the σ_W^2 pattern derived from GRACE data in Fig. 2d. Note that, by considering only spatial correlations, inconsistencies between the total water measured by GRACE and the water amounts allowed by the WBM are avoided.

In analogy to Fig. 6, Fig. 7 shows how S_V varies with imposed combination of $\lambda E/R_{\mathrm{net}}$ and Q/P relationships. The highest skill level appears in Fig. 7c in the cell marked with an X; the corresponding $\lambda E/R_{\mathrm{net}}$ and Q/P relationships are thus those that allow the WBM to best reproduce the observations-based spatial distributions of hydroclimatic variability.

We now define a final skill score, S_T, that identifies the combinations that reproduce well both the means and the variability:

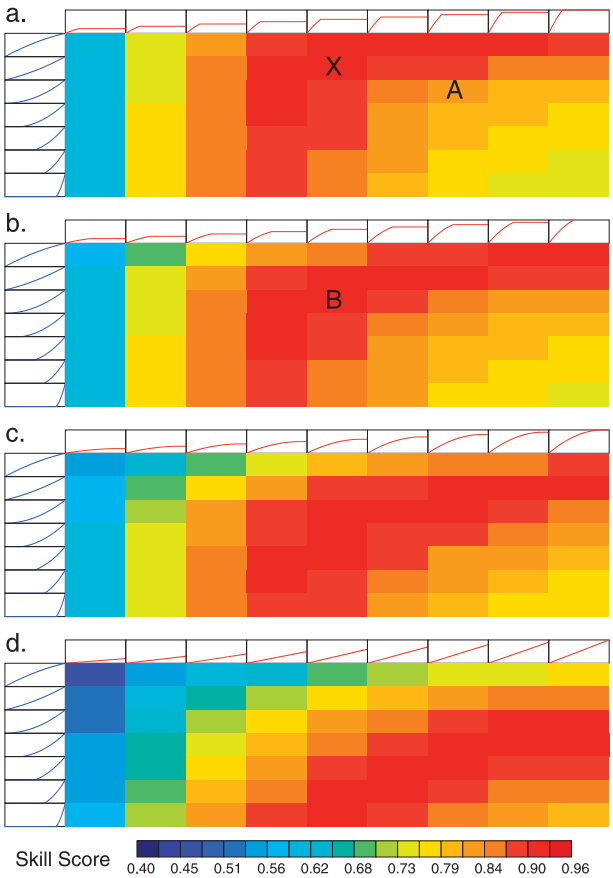

FIG. 6. (a) Variation of the mean skill score 1 minus $\langle \mathrm{RMSE}(Q/P) \rangle$ (see text) as a function of imposed $\lambda E/R_{\mathrm{net}}$ vs W relationship (the red curves along the top of the panel) and imposed Q/P vs W relationship (the blue curves along the left side of the panel). The x axis and y axis for the $\lambda E/R_{\mathrm{net}}$ and Q/P curves span the range (0, 1), as in the leftmost panels of Figs. 3–5. The skill score for a given combination of relationships is indicated by the color of the cell lying in the corresponding column and row. (b)–(d) As in (a) but for a (b) second, (c) third, and (d) fourth set of $\lambda E/R_{\mathrm{net}}$ relationships. Letters mark combinations that are discussed specifically in the text.

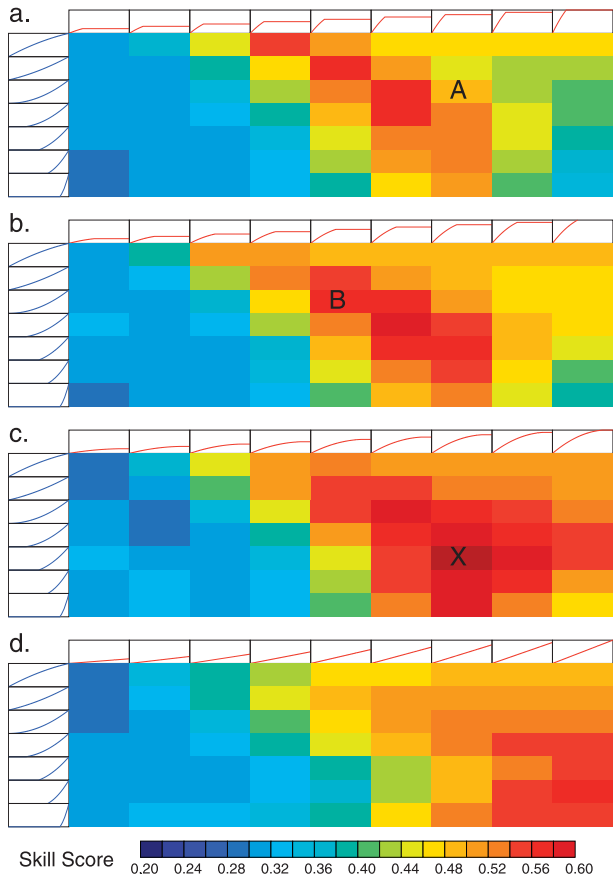

FIG. 7. As in Fig. 6 but for the skill score focusing on hydrological variability, S_V.

$$S_T = S_V + (1 - \langle \mathrm{RMSE}(Q_M/P_M) \rangle); \qquad (4)$$

S_T, which has a maximum value of 2, will only be large if both of its component terms are large.

Results for S_T are shown in Fig. 8. The combination that performs best in the WBM for the joint consideration of means and variability is that corresponding to the cell labeled with an X in the third panel.

We must, of course, be cautious in interpreting this combination as representing the functions that effectively operate in nature, given (i) all of the assumptions underlying the WBM, (ii) that the optimization procedure is simple and subject to the somewhat arbitrary form of (3), and (iii) that several alternative combinations in Fig. 8 also perform well. On the other hand, given that the $\lambda E/R_{\mathrm{net}}$ and Q/P relationships operating in nature have never been measured directly at the large scale, the collection of high-scoring combinations isolated here are of interest. Some indication of how well the identified optimal relationships relate to those operating in the real world is provided in Fig. 9, which compares the observed Q_M/P_M, σ_Q^2, $\sigma_E^2{}^*$, and σ_W^2 fields with those simulated by the WBM using a single pair of optimal functions. The particular set used is that corresponding to the X in Fig. 8. The agreement is certainly not perfect: a particularly egregious difference, for example, is seen for σ_Q^2 in the Ohio River basin (the large basin in the far east), with simulated and observed values of 0.055 $\mathrm{mm}^2\ \mathrm{day}^{-2}$ and 0.11 $\mathrm{mm}^2\ \mathrm{day}^{-2}$, respectively; also, the high simulated σ_W^2 values do not extend far enough into the west. Even so, the observed and simulated fields do show a great many similarities, despite the limited number of degrees of freedom underlying the WBM structure (two parameters each for the $\lambda E/R_{\mathrm{net}}$ and Q/P relationships plus some latitude in choosing the water-holding capacity). The ability of two optimized functions

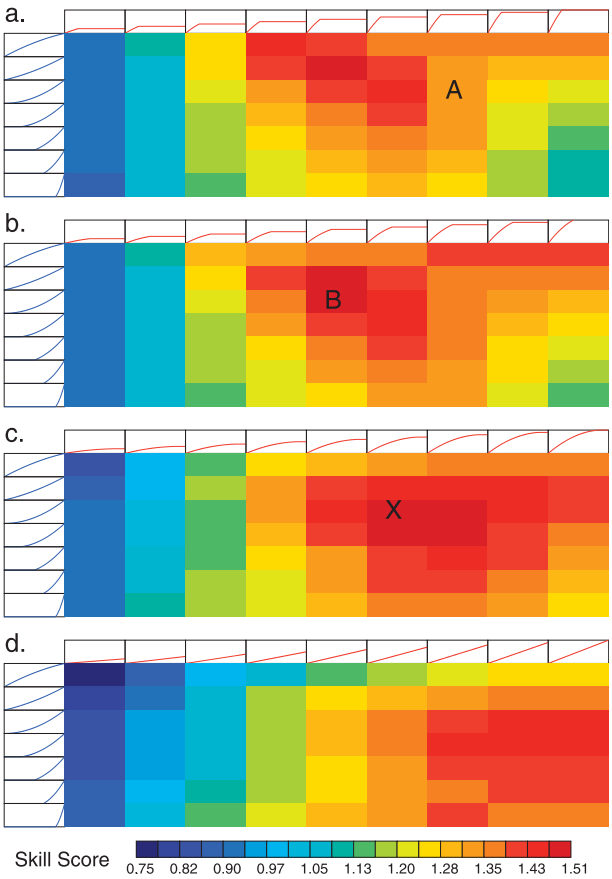

FIG. 8. As in Fig. 6 but for S_T—a skill score focusing on both means and variability.

to capture, to first order, several facets of the observational record in Fig. 9 suggests that the optimized functions do reflect something fundamental about nature.

6. Implications for land surface model development

The WBM used here is, by design, very simple. The usefulness of the sensitivities found above relies wholly on the degree to which the WBM, despite its simplicity, captures the first-order controls imposed by the land surface on large-scale hydroclimatic behavior. We now examine this question using a full land surface model designed for use with numerical climate models. We further demonstrate that the sensitivities uncovered with the WBM can, indeed, guide improvements in the full LSM.

The LSM examined is a recent, developmental version of the Catchment LSM of Koster et al. (2000)—the land component of the earth system model of the NASA/Goddard Space Flight Center (GSFC) Global Modeling and Assimilation Office. The Catchment LSM is like other state-of-the-art LSMs in its consideration of a full range of processes (stomatal conductance, interception, baseflow, snow, etc.) to determine the fluxes that make up the surface energy and water budgets. The model is unique, however, in its treatment of hydrological processes—the land element is divided into time-varying areal fractions defined by topography and water content, and each areal fraction is treated as a separate hydrological regime, with regime-specific treatments of runoff and evaporation processes applied within. The model has been applied and tested in a number of settings (e.g., Ducharne et al. 2000; Boone et al. 2004, Bowling et al. 2003; Reichle et al. 2011). The particular version used here is similar to that used by Li et al. (2012) in its treatment of resistance to bare soil evaporation and hydraulic conductivity decay with depth; this "nonfrozen" version of the model shows room for improvement and is thus appropriate for the present demonstration.

As suggested in section 1, the net effect of the complex, interacting formulations for evaporation in a LSM can be characterized, to first order, by a diagnosed monotonic relationship between soil moisture content and evaporative fraction. This is illustrated in Fig. 10a for the Catchment LSM. The LSM was driven over the CONUS domain at a resolution of 0.5° × 0.5° using the full complement of the University of Washington forcing (Andreadis et al. 2005) for the period 1948–2000, in the manner described for the control simulations of Mahanama et al. (2012). Output from the simulation was averaged over each month during May–September starting in 1948. Each point in Fig. 10a refers to a specific month, year, and location in CONUS; it is located in the plot according to its wilting-point-corrected monthly W (x axis) and its monthly $\lambda E/R_{\mathrm{net}}$ (y axis). The curve drawn through the points was constructed by computing the average of the $\lambda E/R_{\mathrm{net}}$ values over narrow bins of W. (Note that different locations have different minimum W values, as induced by differences in the soil textures assumed by the model. Prior to plotting W for a given point in Fig. 10a, the minimum attainable soil moisture at that point was subtracted from it; this is what is meant here by "wilting-point-corrected" W.)

The Catchment LSM's evaporative fraction function is thus characterized by a curve that increases with W until W (relative to the baseline associated with wilting point) reaches about 0.2, at which point the curve plateaus to a roughly constant level. The scatter about the curve is large, as would be expected given that the Catchment LSM is in fact a complex model. Still, the fitted curve captures its first-order behavior.

The corresponding plot for runoff ratio is presented in Fig. 10b. The scatter here appears larger; this presumably

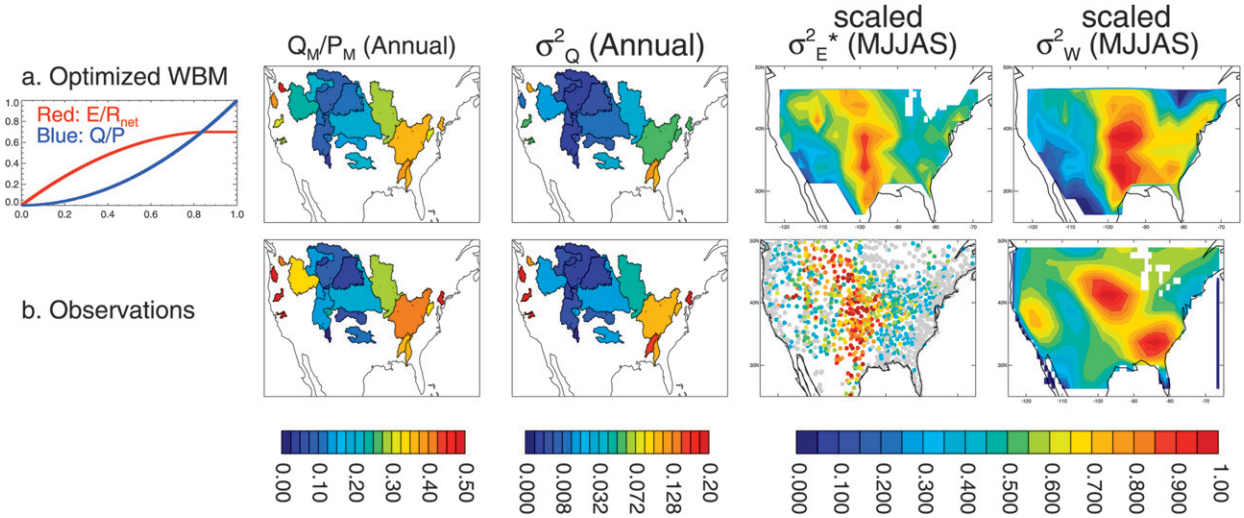

FIG. 9. (a) Simulation of hydroclimatic statistics from the version of the WBM that best reproduces observations (indicated by the box marked with an X in Fig. 8). This row provides, for the indicated pairing of $\lambda E/R_{\mathrm{net}}$ and Q/P relationships, the resulting WBM-derived spatial distributions (from left to right) of the average runoff ratio Q_M/P_M in individual basins (dimensionless), σ_Q^2 in individual basins ($\mathrm{mm^2\ day^{-2}}$), σ_E^2* (no units), and σ_W^2 (no units). Note that σ_E^2* and σ_W^2 are arbitrarily scaled to allow the spatial patterns to be compared with those of the observations. (b) Corresponding hydroclimatic statistics from observations.

reflects the impact of baseflow, which can allow winter and early spring precipitation to run off during warm season months even if precipitation in the latter period is small. Despite the scatter, a clear increase of Q/P with W is seen in the distribution of points, as captured by the fitted curve.

The set of fitted curves in Fig. 10 is now used as the set of prescribed $\lambda E/R_{\mathrm{net}}$ and Q/P relationships in a WBM simulation. The degree to which the WBM thereby captures the behavior of the full LSM is shown in Fig. 11; Figs. 11a and 11b show, respectively, the Catchment-LSM and WBM simulations of Q_M/P_M, σ_Q^2, σ_E^2*, and σ_W^2. (Because of differences in effective water-holding capacity between the LSM and WBM and our focus, in any case, on the spatial distribution of variability, the values of σ_W^2 in each panel are independently and arbitrarily scaled to allow easier comparison.) The agreement in all fields is reasonably strong. The WBM, despite its simple structure, appears to capture the controls of the more complex LSM on hydroclimatic means and variability, reproducing, for example, the swath of high σ_E^2* down the center of the continent and the LSM's magnitudes of Q_M/P_M and σ_Q^2 in almost all of the large-scale basins.

The WBM performance here suggests that the sensitivity results presented in Figs. 6–8 can help guide LSM development. The idea is simple: if a change to the WBM set of $\lambda E/R_{\mathrm{net}}$ and Q/P relationships leads to a more realistic set of hydroclimatic statistics, the corresponding change to the full LSM effective relationships should show a similar benefit. We test this idea now.

The fitted $\lambda E/R_{\mathrm{net}}$ and Q/P relationships in Fig. 10 for the LSM agree most closely with those corresponding to the box labeled A in Figs. 6–8. This combination is seen from these figures to be suboptimal for the WBM. According to Fig. 8, the WBM overall behavior improves (relative to that produced with the combination for box A) if the height of the evaporation function is decreased (i.e., we move leftward from box A in Fig. 8a) or if the transition point between soil-moisture-controlled and energy-limited evaporation increases (i.e., we move from box A to the equivalent location in Figs. 8b, 8c, or 8d). Note that a change to the runoff function cannot by itself lead to an improvement.

These WBM results suggest a simple sensitivity test with the Catchment LSM—we should adjust the LSM evaporation formulation so that its effective $\lambda E/R_{\mathrm{net}}$ function is reduced at all soil moisture levels, and particularly for lower soil moisture levels. In our test, we increase the Catchment LSM resistances to both bare soil evaporation and transpiration in such a way that the fitted, effective evaporation function is transformed from that shown in the first panel of Fig. 12a to that in the first panel of Fig. 12b—a form that has the desired specifications. (The change involves a reworking of certain soil moisture stress terms in the evaporation calculation.) The Catchment LSM runoff parameterization is not changed in the test, and accordingly, the fitted runoff relationship is essentially the same. The new combination of fitted relationships roughly agrees with the combination of relationships corresponding to the box labeled B in Fig.

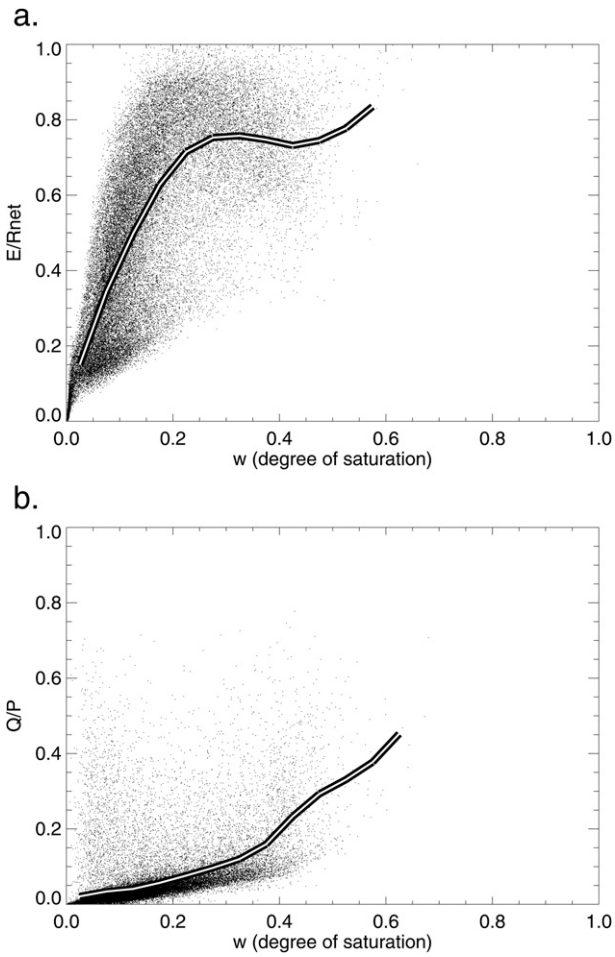

FIG. 10. (a) Scatterplot constructed from a multidecadal simulation over CONUS with the Catchment LSM of Koster et al. (2000). Each dot corresponds to a single grid cell and a single month during May–September of a single year; it is located on the plot according to the mean soil moisture simulated for that location and time period (x axis) and the corresponding simulated evaporative fraction (y axis). The line through the points was constructed via a simple binning procedure. (b) As in (a) but for soil moisture vs runoff ratio.

8b—a combination that should, according to Fig. 8, produce more realistic results.

This is verified in columns 2 through 5 of Fig. 12, which show, respectively, the simulated distributions of Q_M/P_M, σ_Q^2, σ_E^2*, and σ_W^2 from the Catchment LSM (before and after the parameterization change) and the observed distributions. Note again that the evaporation ''observations'' are, in fact, temperature-based proxies so that only the spatial pattern of σ_E^2* is relevant here; we thus scale the values arbitrarily (but uniformly across CONUS) to allow similar shading levels to appear in the different σ_E^2* maps for easier comparison. The GRACE-based σ_W^2 values are similarly scaled.

The improvement in Q_M/P_M, σ_Q^2, and σ_E^2* obtained with the modified LSM (Fig. 12b) is clear. The magnitudes of Q_M/P_M and σ_Q^2 (which are not scaled in the figure) are much more realistic, and the inaccurate band of high σ_E^2* values along the eastern coast of the continent has disappeared—the spatial pattern of σ_E^2* obtained with the modified LSM more closely matches that of the observations. The simulated spatial distribution of σ_W^2 is not obviously improved, though the distribution is spread out more toward the west than before, in agreement with the GRACE data.

7. Summary and discussion

The simple water balance model (WBM) described in section 2, when integrated with several decades of observations-based forcing, generates continental-scale fields of hydroclimatic statistics—namely, mean runoff and the variances of runoff, evaporation, and soil moisture. These Q_M/P_M, σ_Q^2, σ_E^2*, and σ_W^2 fields are seen to be strongly sensitive to changes in the WBM's imposed soil moisture–evapotranspiration and soil moisture–runoff relationships. In accordance with the KM97 findings for mean fluxes, what matters most for both means and variability is the relative positioning of the two relationships; both evaporation and runoff are affected by the two imposed relationships working together. A comparison of Figs. 3 and 5 shows that runoff statistics in the WBM are, in fact, affected more by the imposed evaporation formulation than by the imposed runoff formulation.

Comparisons with observed fields (the absolute magnitudes of Q_M/P_M and the spatial patterns of σ_Q^2, σ_E^2*, and σ_W^2) give an indication of the soil moisture–evapotranspiration and soil moisture–runoff formulations effectively operating in nature, under the assumption that a single pairing of functions can be considered universal. This assumption is naturally flawed; for example, the efficiency of evapotranspiration presumably varies with the character of vegetation, and runoff generation presumably varies with the character of precipitation (e.g., large-scale versus convective) and differs in mountainous versus nonmountainous areas. In fact, when the WBM runoff results are optimized with observations in each basin independently (not shown), the optimal runoff functions for the more mountainous basins do tend to allow a somewhat more efficient production of runoff. Nevertheless, such spatial corrections to the optimal functions appear to be second order. Figure 11 shows, for example, that a single set of functions captures to first order the hydroclimatic statistics produced by a full, state-of-the-art LSM. Furthermore, Fig. 9 indicates that the WBM, using the

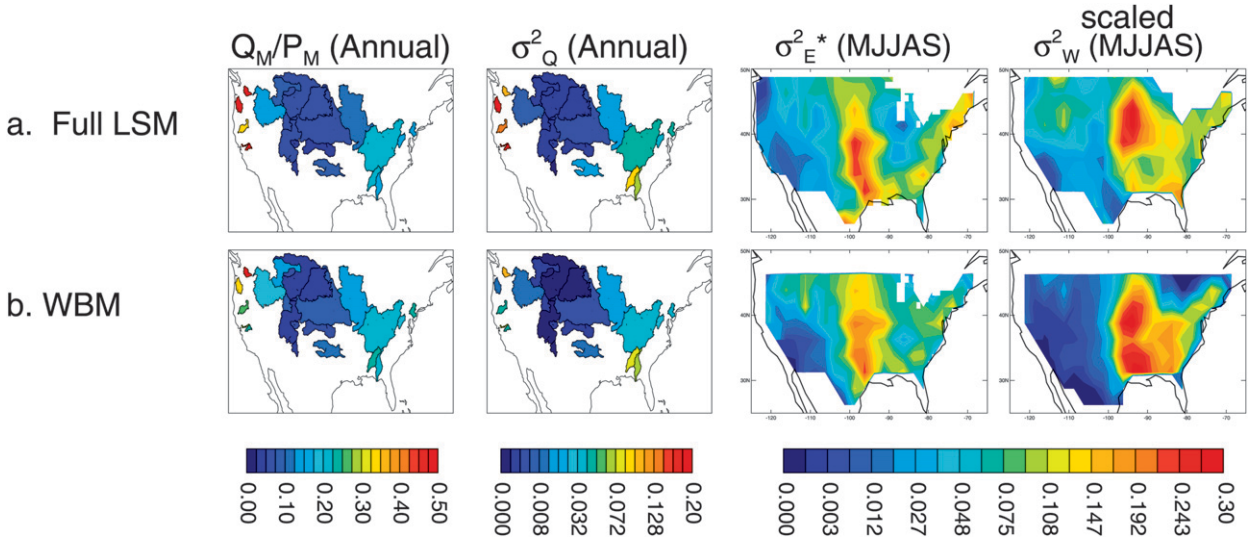

FIG. 11. (a) Hydroclimatic means and variability as generated by a full land surface model. Shown in order (from left to right) are the simulated spatial distributions of Q_M/P_M (dimensionless), σ^2_Q (mm^2/day^2), σ^2_E* (mm^2 day^{-2}), and σ^2_W (no units); note that σ^2_W is arbitrarily scaled in the last panel. (b) As in (a) but for the WBM fitted with the $\lambda E/R_{\rm net}$ and Q/P relationships derived from the full land model, and with a different scaling factor used for σ^2_W.

optimal pairing of functions from Fig. 8, reproduces much of the character of hydroclimatic variability in North America. Overall, the results support the idea that our optimized pairings of functions do represent the functions effectively operating in nature—again, to first order.

The complex relationships between soil moisture, evapotranspiration, and runoff in a land surface component

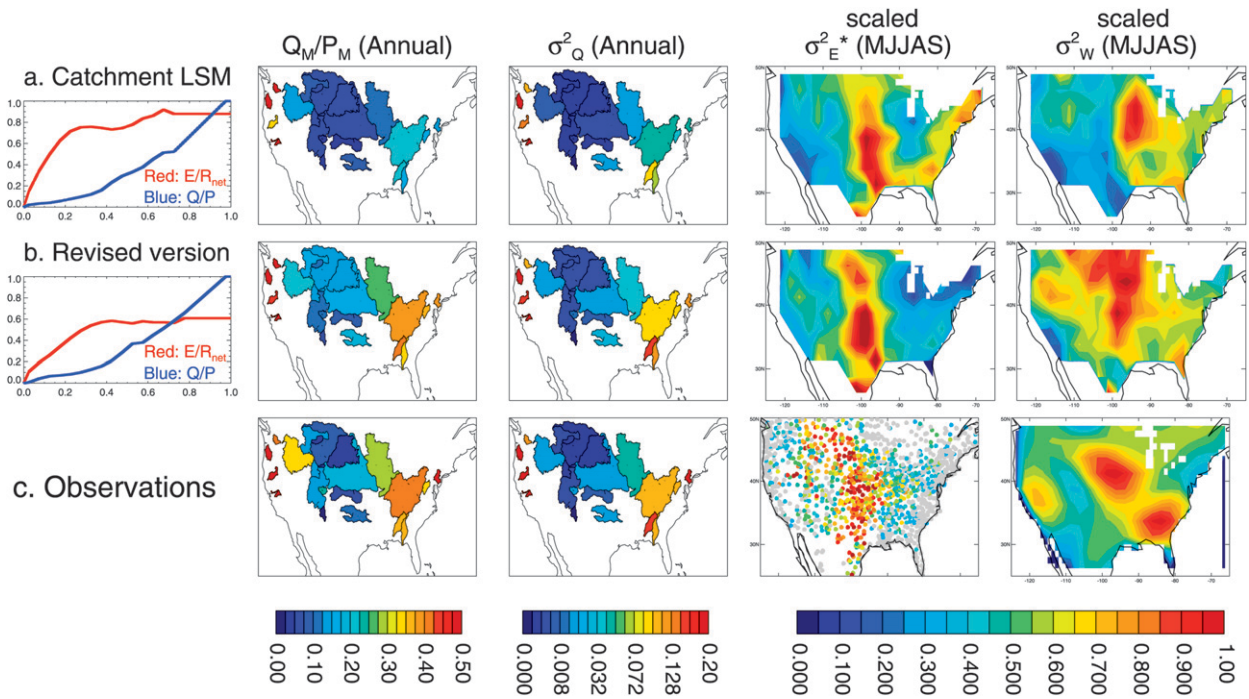

FIG. 12. (a) The average $\lambda E/R_{\rm net}$ and Q/P relationships underlying the full land surface model along with the simulated spatial distributions (from left to right) of Q_M/P_M (dimensionless), σ^2_Q (mm^2 day^{-2}), σ^2_E* (no units), and σ^2_W (no units) produced by the full land surface model. (b) As in (a) but for a revised version of the full land surface model, and with different scaling factors used for σ^2_E* and σ^2_W and (c) observed spatial distributions of Q_M/P_M, σ^2_Q, σ^2_E*, and σ^2_W, from Fig. 2. The values of σ^2_E* or σ^2_W within a given panel are scaled arbitrarily to allow the simulated and observed spatial patterns to be more easily compared.

of a numerical climate model can also be mimicked with the WBM, as demonstrated in Fig. 11. This agreement suggests a framework for LSM development and improvement, one that could supplement more traditional approaches (e.g., evaluation and calibration of an LSM at small spatial scales with flux tower data). A LSM's deficiencies in regard to hydroclimatic simulation can be characterized by its effective position on skill plots such as those in Figs. 6–8, and those skill plots in turn indicate how a LSM's evaporation and/or runoff formulation should be modified to improve its simulation of hydroclimate. The particular version of the Catchment LSM examined in Fig. 12a produced markedly insufficient runoff ratios in the eastern United States. According to Fig. 8, the WBM analog for the LSM could be improved not by adjusting the runoff formulation but by adjusting the soil moisture–evaporation relationship downward to a certain level. A corresponding modification to the LSM produced the desired improvement in hydroclimatic simulation.

The importance of a proper characterization of hydroclimatic means and variability cannot be overemphasized. Hydroclimatic variability is particularly important in the realm of prediction; an improved understanding and simulation of such variability has potential for improvements in short-term and subseasonal weather prediction (Seneviratne et al. 2010) and seasonal streamflow prediction (e.g., Mahanama et al. 2012)—issues of obvious societal relevance. The WBM has been demonstrated here to be a useful tool for investigating controls on this variability and for guiding the development of improved ways to simulate it.

Acknowledgments. This work was supported by the Earth System Science Program of the NOAA/Climate Program Office and by the NASA Terrestrial Hydrology Program. Greg Walker helped with some of the data analyses, and Matt Rodell provided advice on the use of the GRACE data. Radiation data were obtained from the NASA Langley Research Center Atmospheric Sciences Data Center NASA/GEWEX SRB Project. Providers of basin streamflow data include the U.S. Army Corps of Engineers (Omaha and Tulsa offices), the Columbia River Basin Climate Change Scenarios Database, the California Data Exchange Commission, and the U.S. Bureau of Reclamation; Edwin Maurer of Santa Clara University helped obtain additional streamflow data. GRACE land data were processed by Sean Swenson, supported by the NASA MEASURES Program, and are available at http://grace.jpl.nasa.gov.

APPENDIX

Observations-Based Estimate of Evaporation Variability

Seasonally-averaged (MJJAS) temperature is used as a proxy for seasonally-averaged evaporation in the estimation of the spatial pattern of σ_E^2* in Fig. 2c. The seasonal averaging largely smoothes away the effects of other mechanisms that affect temperature variability, such as synoptic-scale weather; at the seasonal scale, evaporation variability remains as the dominant determinant of temperature variability, making the use of the temperature-based proxy possible.

By direct analogy to (1), we characterize the moisture-related variance of the temperature variable T as

$$\sigma_T^2* = \sigma_T^2 r^2(T, P_{\mathrm{ann}}), \tag{A1}$$

where σ_T^2 is the total variance of MJJAS-averaged T and $r^2(T, P_{\mathrm{ann}})$ is the square of the correlation coefficient between MJJAS-averaged T and the total precipitation between October and September. We then assume

$$\sigma_E^2* \sim \sigma_T^2*. \tag{A2}$$

The evaporation–temperature connection is straightforward in regions for which evaporation is soil moisture controlled rather than energy limited (e.g., Seneviratne et al. 2006); evaporation acts to cool the surface, and therefore years with higher MJJAS evaporation should have lower MJJAS surface—and thus air—temperature. In such regions, a higher evaporation variance should lead to a higher temperature variance, and both E and T should show significant correlations with moisture availability (P_{ann}). In regions with energy-limited evaporation, on the other hand, the relationship between evaporation and temperature is more complex; the correlation between them can even be positive. However, in such regions, $r^2(E, P_{\mathrm{ann}})$ (the correlation between evaporation and moisture availability) is, almost by definition, small, and in the absence of a nonevaporation-related mechanism for allowing soil moisture to be correlated with temperature, the same must hold for $r^2(T, P_{\mathrm{ann}})$.

It is appropriate, of course, to point out the caveat that a nonevaporation-related mechanism may, in fact, provide nonzero $r^2(T, P_{\mathrm{ann}})$ or even nonzero $r^2(E, P_{\mathrm{ann}})$ values in energy-limited evaporation regimes. One obvious mechanism to consider is the reduction of incoming radiation associated with higher precipitation. The relevance of this mechanism is reduced here by the use of annual precipitation rather than the

contemporaneous MJJAS precipitation in (A1); we use annual precipitation, by the way, to account for the fact that antecedent precipitation during cooler months, when evaporation is low, can provide water to warm season evaporation through storage in ground reservoirs (Milly 1994). In any case, a modeling study (Koster et al. 2009) provides strong evidence that the radiation mechanism plays a negligible role in controlling seasonal temperature variances.

With this caveat, the product $\sigma_T^2 r^2(T, P_{\mathrm{ann}})$ should increase with the product $\sigma_E^2 r^2(E, P_{\mathrm{ann}})$ in moisture-limited regions, and both products should be near zero in energy-limited regions, supporting the use of (A2). While the units of the two quantities in (A2) differ, their spatial patterns should exhibit common spatial structures, allowing a model-based $\sigma_E^2{}^*$ field to be evaluated via a spatial correlation of the corresponding model-based $\sigma_T^2{}^*$ field with the observational $\sigma_T^2{}^*$ field.

Alternative averaging periods for the precipitation (January–September and April–September) turn out to produce essentially the same $\sigma_T^2{}^*$ fields (not shown). Indeed, an independent modeling analysis suggests that all three averaging periods produce a high degree of correlation of accumulated precipitation with warm season soil moisture, partially reflecting the fact that much of the annual precipitation across the United States falls during the warm season. While small differences in these model results could in principle be used to assign different precipitation accumulation periods to different regions, we utilize annual accumulations both for simplicity and to keep the observations-based estimation of $\sigma_T^2{}^*$ and, thus, $\sigma_E^2{}^*$ completely independent of land model assumptions.

The air temperature and precipitation data used for the $\sigma_T^2{}^*$ calculation are station data from the Global Historical Climatology Network (GHCN) (Peterson and Vose 1997). We examined all stations within North America that satisfy two constraints: (i) the existence of at least 30 years of MJJAS air temperature values and (ii) the coexistence of monthly GHCN precipitation data for the same years, for either the same site or for a station within a few kilometers of the site.

REFERENCES

Andreadis, K. M., E. A. Clark, A. W. Wood, A. F. Hamlet, and D. P. Lettenmaier, 2005: Twentieth-century drought in the conterminous United States. *J. Hydrometeor.,* **6,** 985–1001.

Boone, A., and Coauthors, 2004: The Rhône-Aggregation Land Surface Scheme intercomparison project: An overview. *J. Climate,* **17,** 187–208.

Bowling, L. C., and Coauthors, 2003: Simulation of high-latitude hydrological processes in the Torne–Kalix basin: PILPS Phase 2(e). 1: Experiment description and summary intercomparisons. *Global Planet. Change,* **38,** 1–30.

Budyko, M. I., 1974: *Climate and Life*. Academic Press, 508 pp.

Dirmeyer, P. A., X. Gao, M. Zhao, Z. Guo, T. Oki, and N. Hanasaki, 2006: GSWP-2 multimodel analysis and implications for our perception of the land surface. *Bull. Amer. Meteor. Soc.,* **87,** 1381–1397.

Ducharne, A., R. D. Koster, M. J. Suarez, M. Stieglitz, and P. Kumar, 2000: A catchment-based approach to modeling land surface processes in a general circulation model 2. Parameter estimation and model demonstration. *J. Geophys. Res.,* **105** (D20), 24 823–24 838.

Eagleson, P. S., 1978: Climate, soil, and vegetation: 4. The expected value of annual evapotranspiration. *Water Resour. Res.,* **14,** 731–739.

Guo, Z., P. A. Dirmeyer, Z.-Z. Hu, X. Gao, and M. Zhao, 2006: Evaluation of the Second Global Soil Wetness Project soil moisture simulations: 2. Sensitivity to external meteorological forcing. *J. Geophys. Res.,* **111,** D22S03, doi:10.1029/2006JD007845.

Gupta, S. K., P. W. Stackhouse Jr., S. J. Cox, J. C. Mikovitz, and T. Zhang, 2006: Surface radiation budget project completes 22-year data set. *GEWEX News,* Vol. 16, No. 4, International GEWEX Project Office, Silver Spring, MD, 12–13.

Henderson-Sellers, A., Z.-L. Yang, and R. E. Dickinson, 1993: The Project for Intercomparison of Land-surface Parameterization Schemes. *Bull. Amer. Meteor. Soc.,* **74,** 1335–1349.

Jung, M., and Coauthors, 2010: Recent decline in the global land evapotranspiration trend due to limited moisture supply. *Nature,* **467,** 951–954.

Koster, R. D., and P. C. D. Milly, 1997: The interplay between transpiration and runoff formulations in land surface schemes used with atmospheric models. *J. Climate,* **10,** 1578–1591.

——, and M. J. Suarez, 1999: A simple framework for examining the interannual variability of land surface moisture fluxes. *J. Climate,* **12,** 1911–1917.

——, ——, A. Ducharne, M. Stieglitz, and P. Kumar, 2000: A catchment-based approach to modeling land surface processes in a general circulation model: 1. Model structure. *J. Geophys. Res.,* **105** (D20), 24 809–24 822.

——, P. A. Dirmeyer, P. C. D. Milly, and G. L. Russell, 2001: Comparing GCM-generated land surface water budgets using a simple common framework. *Land Surface Hydrology, Meteorology, and Climate: Observations and Modeling,* V. Lakshmi, J. Albertson, and J. Schaake, Eds., Water Science and Application, Vol. 3, Amer. Geophys. Union, 95–105.

——, M. J. Suarez, R. W. Higgins, and H. M. van den Dool, 2003: Observational evidence that soil moisture variations affect precipitation. *Geophys. Res. Lett.,* **30,** 1241, doi:10.1029/2002GL016571.

——, S. D. Schubert, and M. J. Suarez, 2009: Analyzing the concurrence of meteorological droughts and warm periods, with implications for the determination of evaporative regime. *J. Climate,* **22,** 3331–3341.

Li, B., M. Rodell, B. F. Zaitchik, R. H. Reichle, R. D. Koster, and T. M. van Dam, 2012: Assimilation of GRACE terrestrial water storage into a land surface model: Evaluation and potential value for drought monitoring in Western and Central Europe. *J. Hydrol.,* **446,** 103–115.

Mahanama, S., B. Livneh, R. Koster, D. Lettenmaier, and R. Reichle, 2012: Soil moisture, snow, and seasonal streamflow forecasts in the United States. *J. Hydrometeor.,* **13,** 189–203.

Manabe, S., 1969: Climate and the ocean circulation. I. The atmospheric circulation and the hydrology of the earth's surface. *Mon. Wea. Rev.,* **97,** 739–774.

Milly, P. C. D., 1994: Climate, soil water storage, and the average annual water balance. *Water Resour. Res.,* **30,** 2143–2156.

——, J. Betancourt, M. Falkenmark, R. M. Hirsch, Z. W. Kundzewicz, D. P. Lettenmaier, and R. J. Stouffer, 2008: Stationarity is dead, whither water management? *Science,* **319,** 573–574.

Nemec, J., and J. Schaake, 1982: Sensitivity of water resource systems to climate variation. *Hydrol. Sci. J.,* **3,** 327–343.

Peterson, T. C., and R. S. Vose, 1997: An overview of the global historical climatology network temperature database. *Bull. Amer. Meteor. Soc.,* **78,** 2837–2849.

Reichle, R. H., R. D. Koster, G. J. M. De Lannoy, B. A. Forman, Q. Liu, S. P. P. Mahanama, and A. Toure, 2011: Assessment and enhancement of MERRA land surface hydrology estimates. *J. Climate,* **24,** 6322–6338.

Roderick, M. L., and G. D. Farquhar, 2011: A simple framework for relating variations in runoff to variations in climatic conditions and catchment properties. *Water Resour. Res.,* **47,** W00G07, doi:10.1029/2010WR009826.

Seneviratne, S. I., D. Luthi, M. Litschi, and C. Schar, 2006: Land–atmosphere coupling and climate change in Europe. *Nature,* **443,** 205–209.

——, T. Corti, E. L. Davin, M. Hirschi, E. B. Jaeger, I. Lehner, B. Orlowsky, and A. J. Teuling, 2010: Investigating soil moisture–climate interactions in a changes climate: A review. *Earth Sci. Rev.,* **99,** 125–161.

Swenson, S., and J. Wahr, 2006: Post-processing removal of correlated errors in GRACE data. *Geophys. Res. Lett.,* **33,** L08402, doi:10.1029/2005GL025285.

Tapley, B. D., S. Bettadpur, J. C. Ries, P. F. Thompson, and M. M. Watkins, 2004: GRACE measurements of mass variability in the Earth system. *Science,* **305,** 503–505.

Wood, E. F., and Coauthors, 1998: The Project for Intercomparison of Land-surface Parameterization Schemes (PILPS) Phase 2(c): Red–Arkansas River Basin experiment: 1. Experiment description and summary intercomparisons. *Global Planet. Change,* **19,** 115–135.